Cohesive Zone Interpretations of Phase-field Fracture Models

H. Tran, H.B. Chew*

Department of Aerospace Engineering, University of Illinois at Urbana-Champaign, Urbana IL

61801, USA

*Author to whom all correspondence should be addressed. Email: hbchew@illinois.edu

Abstract

Unlike micromechanics failure models that have a well-defined crack path, phase-field fracture

models are capable of predicting the crack path in arbitrary geometries and dimensions by

utilizing a diffuse representation of cracks. However, such models rely on the calibration of a

fracture energy (G_c) and a regularization length-scale (l_c) parameter, which do not have a strong

micromechanical basis. Here, we construct the equivalent crack-tip cohesive zone laws

representing a phase-field fracture model, to elucidate the effects of G_c and l_c on the fracture

resistance and crack growth mechanics under mode I K-field loading. Our results show that the

cohesive zone law scales with increasing G_c while maintaining the same functional form. In

contrast, increasing l_c broadens the process zone, and results in a flattened traction-separation

profile with a decreased but sustained peak cohesive traction over longer separation distances.

While G_c quantitatively captures the fracture initiation toughness, increasing G_c coupled with

decreasing l_c contributes to a rising fracture resistance curve and a higher steady-state toughness

- both these effects cumulate in an evolving cohesive zone law with crack progression. We

discuss the relationship between these phase field parameters and process zone characteristics in

the material.

Keywords: Phase-field fracture; cohesive zone law; process zone; crack growth; finite element

method

1

1. Introduction

The ability to model and predict crack initiation and propagation in both brittle and ductile solids is pivotal to achieving optimal structural design for fracture resistance. This is especially apparent with the advancement of additive manufacturing technologies which are now capable of rapidly producing material structures of varying complexities [1-3]. Micromechanical failure models typically rely on a local approach, where the fracture event is localized within a well-defined fracture process zone, which is embedded within a continuum constitutive model representing the background material [4,5]. The micromechanisms for fracture, such as void growth and coalescence within the fracture process zone, are modeled either discretely, or through damage constitutive models, such as the Gurson model or cohesive zone laws [6-8]. Such micromechanical models have enabled fundamental studies to elucidate the coupling between complex mechanisms of fracture within the process zone and plastic deformation of the background material [9-11]. A major limitation, however, is that the process zone (and hence the crack path) has to be established a priori [12-17], which complicates the modeling of convoluted crack patterns, including crack branching and merging.

The phase-field approach to fracture departs from the discontinuous description of failure in local micromechanics-based models. The formulation is based on the variational approach of the classical Griffith energy balance for brittle fracture and regularizes the topology of the sharp crack as a diffuse damage zone instead of a discontinuity [18-23]. As such, the model is able to handle topologically complex fractures, and has been widely adopted to solve challenging fracture problems, including hydrogen assisted cracking [24,25], fracture in viscoelastic materials, biomaterials, or anisotropic solids with different material symmetry [26-30], as well as dynamic brittle fracture with complex branching [31,32].

To-date, there is no clear micromechanical basis for the parameters used in the phase-field fracture models. In particular, the amount of crack regularization is controlled through a prescribed length-scale parameter, l_c , which some have perceived as purely a mathematical construct to allow the Griffin crack (Fig. 1a-left) to be smeared over a diffused continuum zone (Fig. 1a-right) [33,34]. In the phase field formulation, l_c arises through a degradation function to describe the material behavior as it transistions between fully intact and damage states. Classical approach for phase field assumes a stifffness-based degradation function, usually in the form of a hyperbole function, as it allows for an accurate reproduction of linear elastic fracture mechanics response [35-37]. In recent years, an energy-based degradation function has been proposed where certain mechanisms of damage can be incorporated directly into the phase field model [38]. For all these degradation functions, the phase field solution should converge to a discrete crack solution in the limit as l_c approaches zero [33]. Others have argued that l_c represents a specific material property that is closely connected to the critical stress for crack nucleation [39-42]. Because of this diffuse crack representation, the fracture energy density term G_c in the phase-field model only approximately relates to the classical Griffith critical energy release rate in the limit of $l_c \rightarrow 0$ [43].

To provide mechanistic insights into the above phase field parameters, one approach is to extract a micromechanics representation of an equivalent fracture process zone of the phase field fracture model through a cohesive zone law. This cohesive zone law constitutes the relationship between interfacial tractions in equilibrium with the surrounding body and the cohesive separations compatible with the deformation fields of the surrounding body [9,10]. A general view is that the cohesive strength (peak traction) and the cohesive energy (area under the traction-separation relation) are the two primary material parameters governing the macroscopic

fracture behavior [13-16]. However, the functional form of the cohesive zone law has been reported to reflect the fracture micromechanisms [44,45]. This has led to the development of inverse techniques to systematically uncover the exact functional form of the cohesive zone laws governed by different failure processes under both monotonic fracture and cyclic fatigue [7,46-49].

In this paper, we explore the relationship between parameters of a phase-field fracture model, and the fracture resistance and crack growth mechanics under mode I loading by investigating the equivalent crack-tip cohesive zone laws representing the phase-field fracture model based on a hyperbole stiffness degradation function. Section 2 describes the finite element implementation of the phase-field fracture model, along with the formulation of a small-scale yielding, modified boundary layer model with imposed monotonic $K_{\rm I}$ remote displacement loading. In Section 3, we systematically study the influence of G_c and I_c on both the macroscopic fracture resistance and microscopic fracture processes as quantified through an equivalent crack-tip cohesive zone law. Section 4 discusses the relationship between these phase field parameters and key process zone characteristics in the material and concludes with a summary.

2. Problem Formulation

2.1 Phase-field fracture modeling

As aforementioned, the formulation of phase field fracture stems from the classical fracture theory of Griffith for a sharp crack with crack surface S in a deformable solid body Ω (Fig. 1a-left), where the energy balance can be formulated in a variational form as

$$\Pi = \int_{\Omega} \psi(u) \, d\Omega + \int_{S} G_{c} \, dS \tag{1}$$

where $\psi(u)$ is the elastic strain energy density as a function of displacement, and G_c is the critical energy release rate characterizing the fracture resistance of the material. Minimizing (1) is not mathematically feasible because of the unknown nature of S. The phase field model overcomes this obstacle by smearing the crack's topology as a diffuse damage zone instead of a discontinuity (Fig. 1a-right). Specifically, the sharp crack is regularized through a diffuse damage variable, ϕ , representing the damage extent caused by the presence of the crack in the surrounding neighborhood, with the limits $\phi = 0$ and 1 representing the intact and fully-cracked regions, respectively [50-52]. Accordingly, (1) can be approximated as [34,53]

$$\Pi = \int_{\Omega} g(\phi)\psi(u)d\Omega + \int_{\Omega} G_c \Gamma_c(\phi, \nabla \phi)d\Omega$$
 (2)

where $g(\phi)$ is a continuous degradation function that monotonically degrades the stiffness of the material as the phase field approaches the crack phase ($\phi = 1$), and is commonly taken as

$$g(\phi) = (1 - \phi)^2 \tag{3}$$

which allows for an accurate reproduction of linear elastic fracture mechanics response [35-37]. The term $\Gamma_c(\phi, \nabla \phi)$ in (2) represents the crack density functional, which enables tracking of the evolving crack surface S. Several crack density functionals have been proposed [35,54,55], and we adopt the form [34]

$$\Gamma_c = \frac{1}{2l_c} \phi^2 + \frac{l_c}{2} |\nabla \phi|^2 \tag{4}$$

where l_c is a regularization length-scale parameter, ensuring that (2) converges to (1) in the limit $l_c \to 0^+$; l_c can be interpreted as a material property in the case of $l_c > 0^+$.

From (2)-(4), the macroscopic equilibrium condition and evolution of phase field equations can be derived, leading to a coupling between the displacement field (u) and the phase field (ϕ)

$$\sigma_{ij,j}(u,\phi) + b_i = 0$$

$$G_c(\frac{\phi}{l_c} - \nabla^2 \phi) - 2(1 - \phi)\psi(u) = 0$$
(5)

where b_i is the body force term, with the Cauchy stress, σ_{ij} , related to the elastic strain, ε_{ij} , and the 4th order elasticity (stiffness) tensor, C_{ijkl} , by

$$\sigma_{ij} = \frac{\partial \Pi}{\partial \varepsilon_{ij}} = g(\phi) C_{ijkl} \varepsilon_{kl} \tag{6}$$

By expressing (5) in a weak form, we discretize (u, ϕ) in a standard finite element scheme, and formulate the residuals and the stiffness matrices. This numerical implementation is described in detail in [24], and is conducted within a user element subroutine in the commercial finite element software, Abaqus.

2.2 Boundary value problem

Our small-scale yielding finite element model contains a semi-infinite "centerline crack" in an isotropic, homogeneous material governed by the phase-field constitutive relation in (6), with elastic modulus E and Poisson's ratio v, and subjected to remote mode I (K_1) loading under plane strain conditions (Fig. 1b). Due to geometrical-symmetry about the x_2 -axis, we model only one-half of the geometry, as shown by the finite element mesh in Fig. 1c. Rather than creating a physical crack, we introduce the crack by setting the phase-field parameter $\phi = 1$ on the row of elements along $x_1 < 0$, $x_2 = 0$. The initial crack-tip, located at $x_1 = x_2 = 0$, is within a highly refined mesh comprising of uniformly-sized elements, each of dimensions $D \times D$, as shown by close-up view of the finite element mesh in Fig. 1d. We impose roller boundary conditions at the start of the dense mesh region (i.e., $x_1 \ge -20D$) along $x_2 = 0$. Along the remote semi-circular boundary of the finite element mesh (Fig. 1c), we prescribe the elastic asymptotic in-plane displacement fields

$$u_1(R,\theta) = K_{\rm I} \frac{1+\nu}{E} \sqrt{\frac{R}{2\pi}} (3 - 4\nu - \cos\theta) \cos\frac{\theta}{2}$$

$$u_2(R,\theta) = K_{\rm I} \frac{1+\nu}{E} \sqrt{\frac{R}{2\pi}} (3 - 4\nu - \cos\theta) \sin\frac{\theta}{2}$$
(7)

where $R^2 = x_1^2 + x_2^2 \approx 40,000D$ and $\theta = \tan^{-1}(\frac{x_2}{x_1})$ for points on the remote boundary. The energy release rate or *J*-integral is related to the mode I stress intensity factor K_I by

$$\Gamma = \frac{1 - \nu^2}{E} K_{\rm I}^2 \tag{8}$$

3. Results

From dimensional analysis, both the macroscopic fracture resistance, Γ , in (8), and the spatial distribution of microscopic field quantities, σ_{ij}/E and ϕ , depend on the following dimensionless geometric-material parameters $\left(\frac{\Gamma}{ED}, \nu, \frac{G_c}{ED}, \frac{l_c}{D}\right)$. In this study, we set $\nu = 0.3$, and direct attention to the phase-field related parameters $\left(\frac{G_c}{ED}, \frac{l_c}{D}\right)$. Note that l_c was originally introduced as a mathematical construct to transform a discrete crack surface into smooth continuum gradient parameters to represent a smeared (diffuse) crack (Fig. 1a), implying that $(2) \rightarrow (1)$ and G_c approaches the fracture toughness only in the limit of $l_c \rightarrow 0$. However, convergence studies show that larger (finite) values of l_c are often required for the phase-field fracture models to match experimental results [24-28,56-58], suggesting that (l_c, G_c) can be regarded as phenomenological material properties. In the following, we will parametrically vary $G_c/(ED)$ from 0.005 to 0.03, and l_c/D from 4 to 14, to elucidate the effects of these phase-field parameters on both the microscopic crack growth processes and the macroscopic fracture resistance. For all our calculations, we define the current crack-tip location as the furthest distance along $x_2 = 0$ where $\phi = 1$.

3.1 Fracture resistance and crack growth process

Fig. 2 shows the effects of G_c and l_c on the fracture resistance (R-) curves. For all cases, G_c (value denoted by square symbols) quantitatively captures the fracture initiation toughness, $\Gamma_{\rm ini}$, as defined by the energy release rate or J-integral (Γ in (8)) at the first instance of crack growth ($\Delta a = D$). The initial crack growth is characterized by the rapid rise in Γ . The rate of increase of Γ slows down significantly for crack growth beyond about 10D, but the continued rise of Γ with Δa beyond this point suggests the continued toughening of the background material, albeit at rates that depend on both l_c/D and $G_c/(ED)$. As shown in Fig. 2b, increasing l_c/D from 4 to 14 at a prescribed $G_c/(ED) = 0.015$ decreases the rate of increase of Γ by $\sim 50\%$. Comparatively, reducing $G_c/(ED)$, and hence $\Gamma_{\rm ini}$, from 0.03 to 0.005 at a fixed $l_c/D = 4$ in Fig. 2a, decreases the rate of increase of Γ by several-folds.

To elucidate the toughening mechanisms associated with the phase-field parameters, G_c and I_c , we show in Fig. 3 contours of the von Mises stress, σ_e , and the phase-field damage variable, ϕ , for three combinations of $G_c/(ED)$ and I_c/D , and at three crack growth instances, $\Delta a/D = 5$, 40, and 80. Comparison between $G_c/(ED) = 0.03$ versus 0.015 at $I_c/D = 4$ shows that the stresses at the crack-tip are notably larger at higher $G_c/(ED)$ across all $\Delta a/D$, with the maximum von Mises stress increasing by nearly two-fold. Interestingly, the contours for ϕ remain almost unchanged. By contrast, increasing I_c/D from 4 to 14 but at a fixed $G_c/(ED) = 0.015$ dramatically increases the width of the diffuse damage zone ϕ . This smearing of damage over a wider region also corresponds with an almost two-fold decrease in the maximum von Mises stress.

As previously shown in Fig. 2, $G_c/(ED)$ is a quantitative measure of the fracture initiation toughness. In addition, the higher von Mises stress-fields surrounding the propagating crack at higher G_c in Fig. 3 suggests that increasing G_c also increases the stress-carrying capacity ahead of the growing crack, which ultimately leads to improved fracture resistance over the entire transient crack growth regime. On the other hand, l_c/D can be interpreted as a measure of the thickness of the fracture process zone defined by $\phi > 0$. As shown in Fig. 3, a larger l_c/D corresponds to a larger and more diffused process zone, while a smaller l_c/D results in a narrower process zone. Since the material stiffness monotonically degrades with $g(\phi)$ in (3) for $\phi > 0$, the reduced stress-carrying capacity in the process zone ahead of the crack-tip at higher l_c/D results in lower fracture resistance. These effects of G_c and I_c are qualitatively in agreement with the stress-strain response of a homogeneously-deformed 1D material with $\nabla \phi = 0$, which shows that the failure stress scales with $\sqrt{G_c/l_c}$ [23,42,59].

Both the contours of σ_e and ϕ in Fig. 3 are evolving with $\Delta a/D$, inferring that the process zone is still developing with crack propagation. This change in near-tip condition with the transition from crack initiation to crack growth is responsible for the rising R-curves in Fig. 2. We show in Fig. 4 the evolution of the near-tip process zone by centering the contours of ϕ about the current crack-tip. Similar contours of ϕ (process zone sizes) are observed between $G_c/(ED)=0.03$ and 0.015 with $l_c/D=4$. In both cases, the damage contours are continuously expanding at a near constant rate as the crack propagates from $\Delta a=5D$ to 80D. In contrast, the contours of ϕ for $G_c/(ED)=0.015$ with $l_c/D=14$ are nearly two- to three-fold larger. A comparatively smaller increase in process zone size is also observed as the crack grows from $\Delta a/D=5D$ to 40D versus $\Delta a/D=40D$ to 80D, indicating that the crack growth is reaching its steady-state.

3.2 Crack-tip cohesive zone laws

Unlike local micromechanics models where damage is confined to a narrow process zone ahead of the crack [5], diffuse nonlocal approaches such as the phase-field fracture model dissipate damage over a wider region and across many elements as shown in Figs. 3 and 4 [12,60,61]. To provide a homogenized view of the diffuse crack-tip process in the phase-field fracture model, we construct the equivalent local traction-separation relationship constituting the cohesive zone law embedded within a linear elastic background material. Figs. 5 and 6 show the effects of $G_c/(ED)$ and l_c/D on the distributions of the crack-tip cohesive tractions, t_2 , cohesive separations, δ_2 , and the phase-field damage parameter, ϕ , at $\Delta a/D=25$. Both $t_2(x_1)$ and $\phi(x_1)$ are obtained directly from the phase-field finite element calculations along $x_2 = 0$. To obtain the equivalent cohesive separation distributions in a linear elastic background material, we impose the measured $t_2(x_1)$ along $x_2 = 0$ of the same finite element mesh with the same K-field displacements as boundary conditions, albeit with a linear elastic (i.e., non-phase-field) constitutive relationship of the same E and ν , and compute $\delta_2(x_1) = 2u_2(x_1)$ along $x_2 = 0$. In this fashion, we effectively project the diffuse damage ϕ within the finite process zone onto a zero-thickness cohesive zone embedded within a linear elastic body, as shown schematically in the inset of Fig. 5b.

Increasing l_c/D with the same $G_c/(ED)$ (Fig. 6a) is found to reduce the peak cohesive tractions. All post-peak traction distributions, however, converge to the same path further ahead of the crack-tip. In contrast, increasing $G_c/(ED)$ with the same l_c/D (Fig. 5a) proportionally increases both the peak and post-peak traction distributions, while maintaining the same traction distribution profile. Increasing $G_c/(ED)$ causes a pronounced increase in the crack-tip separations versus the effects of l_c/D (compare Fig. 5b versus Fig. 6b). However, increasing

 l_c/D also increases the length of the crack-tip cohesive zone, as evidenced by both the larger non-zero separations (Fig. 6b) and the slower decay of damage (Fig. 6c) further ahead of the crack-tip. In comparison, increasing $G_c/(ED)$ has negligible influence on the cohesive zone size – the separation and damage distributions (Figs. 5b and 5c) both decay to zero at nearly-identical distances ahead of the crack-tip.

Together, the above cohesive traction (Figs. 5a and 6a) and separation (Figs. 5b and 6b) distributions are used to construct the traction-separation relationships in Fig. 7 constituting the crack-tip cohesive zone laws in a linear elastic background material. Generally, the cohesive strength (peak cohesive traction) and the cohesive energy [area under the (t_2, δ_2) envelope] are two important variables which control the fracture resistance. While $G_c/(ED)$ corresponds to the fracture initiation toughness, Γ_{ini} , the cohesive energy here quantitatively corresponds to the fracture resistance Γ at the specific crack instant where the cohesive zone law was constructed $(\Delta a/D = 25)$. As shown in Fig. 7a, increasing $G_c/(ED)$ increases both the cohesive strength and energy, but the functional form of the cohesive traction-separation relationship remains the same. Increasing l_c/D in Fig. 7b decreases the cohesive strength, and to a lesser extent, the cohesive energy. More importantly, a significant change in the functional form of the cohesive zone law is observed - from a rapid increase and subsequent decrease in cohesive tractions at short separation distances for $l_c/D=4$ to the flattening of the cohesive zone law resulting in a sustained, but lower, peak traction over longer separation distances (i.e., longer cohesive zone) for $l_c/D = 14$. These changes in shape of the cohesive zone law with l_c/D can be used to represent changes in the fracture micromechanisms.

In the phase field model, the damage parameter ϕ provides a measure of the transition from an undamaged ($\phi = 0$) to a fully-cracked ($\phi = 1$) material. An alternative "cohesive zone"

approach to quantify crack growth is to consider the cohesive energy dissipated as the separation progresses, as quantified by the evolving area encompassed by the traction-separation response, i.e., $\Gamma_s(\delta_2) = \int_0^{\delta_2} t_2(\delta_2') \, d\delta_2'$, relative to the separation energy Γ . Thus, $\Gamma_s/\Gamma = 0$ at $\delta_2 = 0$ represents a fully-intact material, while $\Gamma_s/\Gamma = 1$ when the cohesive zone is fully-developed at $\delta_2 = \delta_0$ (inset in Fig. 5b) denotes a fully-separated material. A comparison of the evolution of ϕ (red) and Γ_s/Γ (black) with δ_2 across various (l_c , G_c) combinations in Fig. 8 demonstrates that the damage or crack growth assessment from both approaches are in good quantitative agreement.

The rising R-curves in Fig. 2 suggest that the cohesive zone law is evolving as the crack propagates. Accordingly, we show in Fig. 9 the evolving cohesive zone laws reconstructed from the traction and separation distributions at increasing $\Delta a/D$ across various l_c and G_c combinations. Note that the cohesive energy of each of these $(l_c, G_c, \Delta a)$ combinations are quantitatively in perfect agreement with the calculated energy releases rate, $\Gamma(\Delta a/D)$, in Fig. 2, since all of the dissipation energy in the process zone is projected onto an equivalent zero-thickness cohesive zone. While the shape of the cohesive zone law generally remains unchanged, increasing $\Delta a/D$ increases both the peak cohesive traction as well as the total separation, δ_0 , particularly at high $G_c/(ED)$ of 0.025 where a 16% increase in the cohesive strength is observed as the crack propagates from $\Delta a/D = 10$ to 115. At higher l_c/D , the cohesive zone laws rapidly converge with $\Delta a/D$, indicating a transition to steady-state crack growth.

4. Discussions and Conclusion

In the micromechanics modeling of fracture, a brittle or ductile fracture response often correlates with the extent of plastic dissipation in the background material. In the case of brittle fracture, damage is often confined to the thin process zone ahead of the crack, and the limited plastic dissipation results in a flat R-curve representing rapid and unstable crack propagation. In the case of ductile fracture, the development of significant background plastic dissipation results in a rising R-curve. The phase-field fracture model we have adopted is widely considered to be "brittle" as we have assumed an elastic background material. We remark that "ductile" phase-field fracture models based on elasto-plastic background materials have also been proposed in the open literature [36,56,57,62,63]. However, our crack growth simulations for this "brittle" phase-field fracture model demonstrate a rising R-curve in cases with large G_c and/or small l_c , suggesting that this seemingly "brittle" model can effectively simulate the fracture response of ductile materials.

Akin to crack growth in an elasto-plastic material, the macroscopic fracture resistance Γ in our phase-field model can be delineated into two primary contributions: the fracture initiation toughness, $\Gamma_{\rm ini}$, and phase-field dissipation energy, Γ_p . Our simulation results in Fig. 2 show that G_c is a direct quantitative measure of $\Gamma_{\rm ini}$, in agreement with prior studies [42,53], while both G_c and I_c have profound effects on Γ_p . Similar to the growth of the plastic zone size during transient crack growth, the transition from crack initiation to steady-state crack growth in our phase-field fracture model is marked by the development of a diffuse damage zone which evolves with Δa (Figs. 3 and 4). This diffuse zone can be treated as an *evolving* fracture process zone in the transient crack growth regime, and is distinct from micromechanics fracture models which almost always assume a fixed process zone size.

One approach to quantify the phase-field fracture process is to project the diffuse damage into an equivalent crack-tip cohesive zone law which evolves with crack growth. In doing so, the cohesive energy quantitatively equates to the total fracture resistance, $\Gamma(\Delta a)$, which

encompasses both the contributions of $\Gamma_{\rm ini}$ and $\Gamma_p(\Delta a)$. Our results in Figs. 5-7 show that G_c has a strong influence on both the cohesive strength and cohesive energy, but has negligible effects on the shape of the cohesive zone law – this suggests that the underlying crack growth mechanics remain unchanged with G_c . In contrast, l_c significantly changes the functional form of the cohesive zone law, and a transition from a sharp traction-separation profile resembling a bilinear cohesive zone model to a flattened traction-separation profile resembling a trapezoidal cohesive zone model is observed with increasing l_c . This change in the shape of the traction-separation relationship is associated with the increasing size of the diffuse damage zone with l_c – a larger l_c creates both a thicker and longer fracture process zone with reduced cohesive strength. By comparison, increasing G_c has negligible influence on the process zone size.

Our studies, therefore, demonstrate that l_c quantitatively relates to the size of the fracture process zone. In the limit of $l_c \to 0$, the process zone physically collapses to a zero-thickness cohesive zone, and the phase-field fracture model would indeed be equivalent to a sharp crack propagating within an elastic medium. The fracture process would always be brittle with $\Gamma = G_c$, since there would be no energy dissipation in the background material. However, convergence studies often lead to the adoption of relatively large values of $l_c/D > 10$ [24,25,29,62], which introduces a finite thickness fracture process zone. Differing from these numerical studies, our results suggest that l_c should be calibrated and selected based on the physical thickness of the fracture process zone. For example, a small value of l_c/D should be used to represent the narrow process zone for cracking in a brittle rock-like material such as shale or concrete [64,65], while a larger l_c/D will better represent the more diffused process zone associated with micro-crazing in polymers [66,67]. This would provide l_c/D with a stronger physical basis. The "brittle" phase-field fracture model we adopt does not account for background plasticity. Without loss of

generality, our simulations suggest that the background plastic dissipation in elasto-plastic materials constituting Γ_p can heuristically be treated as a diffuse damage zone represented by appropriately calibrated values of l_c/D .

The cohesive strength within the process zone depends on both G_c and I_c . Uniform deformation studies show that the critical strength in the stress-strain response of a phase-field element scales with $\sqrt{G_c/I_c}$ [23,42,59], and the cohesive strength of our equivalent crack-tip cohesive zone laws appear to follow similar trends. Conceivably, once I_c is calibrated to represent the size of the fracture process zone, G_c can in turn be calibrated to fit the cohesive strength representing the appropriate crack growth mechanisms, such as void growth and coalescence, fiber pull-out, and phase transformation.

In conclusion, we have obtained new physical insights into the role of the energy and length-scale parameters, G_c and l_c , in phase-field fracture models, by constructing the equivalent crack-tip cohesive zone laws representative of the diffuse damage process. We demonstrate that G_c can be perceived as the fracture initiation toughness, and quantitatively controls both the cohesive strength and energy. While l_c was initially introduced as a mathematical construct, we show that l_c should be physically interpreted as a measure of the thickness of the diffuse damage (fracture process) zone. By adopting finite values of l_c , together with appropriately-calibrated values of G_c , the "brittle" phase-field fracture model can be used to simulate a wide variety of material systems, from brittle rock materials with narrow process zones to ductile metals with diffuse background plastic dissipation. We remark that a commonly used stiffness-based hyperbole degradation function is considered in this study. Extracting the equivalent cohesive zone laws for other degradation functions is a subject of future work.

Acknowledgements

The authors acknowledge the support provided by National Science Foundation under Grant Nos. NSF-CMMI-2009684 and NSF-DMR-18-09696.

References

- [1] Foehring, D., Chew, H.B., & Lambros, J. (2018). Characterizing the tensile behavior of additively manufactured Ti-6Al-4V using multiscale digital image correlation. *Materials Science and Engineering*, A 724, 536-546.
- [2] Liu, S., & Shin, Y. C. (2019). Additive manufacturing of Ti6Al4V alloy: A review. *Materials & Design*, 164, 107552.
- [3] VanSickle, R., Foehring, D., Chew, H.B., & Lambros, J. (2020). Microstructure effects on fatigue crack growth in additively manufactured Ti-6Al-4V. *Materials Science and Engineering*, A 795, 139993.
- [4] Tvergaard, V., & Hutchinson, J. W. (1992). The relation between crack growth resistance and fracture process parameters in elastic-plastic solids. *Journal of the Mechanics and Physics of Solids*, 40(6), 1377–1397.
- [5] Hutchinson, J. W., & Evans, A. G. (2000). Mechanics of materials: Top-down approaches to fracture. *Acta Materialia*, 48(1), 125–135.
- [6] Chew, H. B., Guo, T. F., & Cheng, L. (2005). Vapor pressure and residual stress effects on failure of an adhesive film. *International Journal of Solids and Structures*, 42(16), 4795–4810.
- [7] Cui, Y., Gao, Y. F., & Chew, H. B. (2020). Two-scale porosity effects on cohesive crack growth in a ductile media. *International Journal of Solids and Structures*, 200–201, 188–197.
- [8] Muro-Barrios, R., Cui, Y., Lambros, J., & Chew, H. B. (2022). Dual-scale porosity effects on crack growth in additively manufactured metals: 3D ductile fracture models. *Journal of the Mechanics and Physics of Solids*, 159, 104727.
- [9] Barenblatt, G. I. (1962). The Mathematical Theory of Equilibrium Cracks in Brittle Fracture. In H. L. Dryden, Th. von Kármán, G. Kuerti, F. H. van den Dungen, & L. Howarth (Eds.), *Advances in Applied Mechanics* (Vol. 7, pp. 55–129). Elsevier.
- [10] Dugdale, D. S. (1960). Yielding of steel sheets containing slits. *Journal of the Mechanics and Physics of Solids*, 8(2), 100–104.
- [11] Xia, L., & Shih, C. F. (1995). Ductile crack growth-I. A numerical study using computational cells with microstructurally-based length scales. *Journal of the Mechanics and Physics of Solids*, 43(2), 233–259.
- [12] Linder, C., & Armero, F. (2007). Finite elements with embedded strong discontinuities for the modeling of failure in solids. *International Journal for Numerical Methods in Engineering*, 72(12), 1391–1433.
- [13] Chen, C. R., Kolednik, O., Scheider, I., Siegmund, T., Tatschl, A., & Fischer, F. D. (2003). On the determination of the cohesive zone parameters for the modeling of micro-ductile crack growth in thick specimens. *International Journal of Fracture*, 120(3), 517–536.
- [14] Gustafson, P. A., & Waas, A. M. (2009). The influence of adhesive constitutive parameters in cohesive zone finite element models of adhesively bonded joints. *International Journal of Solids and Structures*, 46(10), 2201–2215.

- [15] Desai, C. K., Basu, S., & Parameswaran, V. (2016). Determination of Traction Separation Law for Interfacial Failure in Adhesive Joints at Different Loading Rates. *The Journal of Adhesion*, 92(10), 819–839.
- [16] Jemblie, L., Olden, V., & Akselsen, O. M. (2017). A review of cohesive zone modelling as an approach for numerically assessing hydrogen embrittlement of steel structures. *Philosophical Transactions of the Royal Society A: Mathematical, Physical and Engineering Sciences*, 375(2098), 20160411.
- [17] Lélias, G., Paroissien, E., Lachaud, F., & Morlier, J. (2019). Experimental characterization of cohesive zone models for thin adhesive layers loaded in mode I, mode II, and mixed-mode I/II by the use of a direct method. *International Journal of Solids and Structures*, 158, 90–115.
- [18] Peerlings, R. H. J., Borst, R., Brekelmans, W. A. M., Vree, J. H. P., & Spee, I. (1996). Some observations on localization in non-local and gradient damage models. *European Journal of Mechanics*. *A, Solids*, *15*(6), 937–953.
- [19] Peerlings, R. H. J., de Borst, R., Brekelmans, W. a. M., & Geers, M. G. D. (1998). Gradient-enhanced damage modelling of concrete fracture. *Mechanics of Cohesive-Frictional Materials*, *3*(4), 323–342.
- [20] Comi, C. (1999). Computational modelling of gradient-enhanced damage in quasi-brittle materials. *Mechanics of Cohesive-Frictional Materials*, 4(1), 17–36.
- [21] Lorentz, E., & Andrieux, S. (2003). Analysis of non-local models through energetic formulations. *International Journal of Solids and Structures*, 40(12), 2905–2936.
- [22] Benallal, A., & Marigo, J.-J. (2006). Bifurcation and stability issues in gradient theories with softening. *Modelling and Simulation in Materials Science and Engineering*, 15(1), S283–S295.
- [23] Marigo, J.-J., Maurini, C., & Pham, K. (2016). An overview of the modelling of fracture by gradient damage models. *Meccanica*, 51(12), 3107–3128.
- [24] Martínez-Pañeda, E., Golahmar, A., & Niordson, C. F. (2018). A phase field formulation for hydrogen assisted cracking. *Computer Methods in Applied Mechanics and Engineering*, 342, 742–761.
- [25] Kristensen, P. K., Niordson, C. F., & Martínez-Pañeda, E. (2020). Applications of phase field fracture in modelling hydrogen assisted failures. *Theoretical and Applied Fracture Mechanics*, 110, 102837.
- [26] Teichtmeister, S., Kienle, D., Aldakheel, F., & Keip, M.-A. (2017). Phase field modeling of fracture in anisotropic brittle solids. *International Journal of Non-Linear Mechanics*, 97, 1–21.
- [27] Carollo, V., Guillén-Hernández, T., Reinoso, J., & Paggi, M. (2018). Recent advancements on the phase field approach to brittle fracture for heterogeneous materials and structures. *Advanced Modeling and Simulation in Engineering Sciences*, 5(1), 8.
- [28] Li, S., Tian, L., & Cui, X. (2019). Phase field crack model with diffuse description for fracture problem and implementation in engineering applications. *Advances in Engineering Software*, 129, 44–56.
- [29] Wu, J. (2017). A unified phase-field theory for the mechanics of damage and quasi-brittle failure. *Journal of the Mechanics and Physics of Solids*, 103, 72-99.
- [30] Yin, B., Storm, J., & Kaliske, M. (2021). Viscoelastic phase-field fracture using the framework of representative crack elements. *International Journal of Fracture*.

- [31] Borden, M. J., Verhoosel, C. V., Scott, M. A., Hughes, T. J. R., & Landis, C. M. (2012). A phase-field description of dynamic brittle fracture. *Computer Methods in Applied Mechanics and Engineering*, 217–220, 77–95.
- [32] Liu, G., Li, Q., Msekh, M. A., & Zuo, Z. (2016). Abaqus implementation of monolithic and staggered schemes for quasi-static and dynamic fracture phase-field model. *Computational Materials Science*, 121, 35–47.
- [33] Braides, A. (1998). A general approach to approximation. In A. Braides (Ed.), *Approximation of Free-Discontinuity Problems* (pp. 87–102). Springer.
- [34] Bourdin, B., Francfort, G. A., & Marigo, J.-J. (2000). Numerical experiments in revisited brittle fracture. *Journal of the Mechanics and Physics of Solids*, 48(4), 797–826.
- [35] Borden, M. J., Hughes, T. J. R., Landis, C. M., & Verhoosel, C. V. (2014). A higher-order phase-field model for brittle fracture: Formulation and analysis within the isogeometric analysis framework. *Computer Methods in Applied Mechanics and Engineering*, 273, 100–118.
- [36] Borden, M. J., Hughes, T. J. R., Landis, C. M., Anvari, A., & Lee, I. J. (2016). A phase-field formulation for fracture in ductile materials: Finite deformation balance law derivation, plastic degradation, and stress triaxiality effects. *Computer Methods in Applied Mechanics and Engineering*, 312, 130–166.
- [37] Pham, K., Amor, H., Marigo, J.-J., & Maurini, C. (2011). Gradient Damage Models and Their Use to Approximate Brittle Fracture. *International Journal of Damage Mechanics*, 20(4), 618–652.
- [38] Wu, C., Fang, J., Zhang, Z., Entezari, A., Sun, G., Swain, M. V., & Li, Q. (2020). Fracture modeling of brittle biomaterials by the phase-field method. *Engineering Fracture Mechanics*, 224, 106752.
- [39] Bourdin, B., Marigo, J.-J., Maurini, C., & Sicsic, P. (2014). Morphogenesis and propagation of complex cracks induced by thermal shocks. *Physical Review Letters*, 112(1).
- [40] Mesgarnejad, A., Bourdin, B., & Khonsari, M. M. (2015). Validation simulations for the variational approach to fracture. *Computer Methods in Applied Mechanics and Engineering*, 290, 420–437.
- [41] Nguyen, T. T., Yvonnet, J., Bornert, M., Chateau, C., Sab, K., Romani, R., & Le Roy, R. (2016). On the choice of parameters in the phase field method for simulating crack initiation with experimental validation. *International Journal of Fracture*, 197(2), 213–226.
- [42] Tanné, E., Li, T., Bourdin, B., Marigo, J.-J., & Maurini, C. (2018). Crack nucleation in variational phase-field models of brittle fracture. *Journal of the Mechanics and Physics of Solids*, 110, 80–99.
- [43] Francfort, G. A., & Marigo, J.-J. (1998). Revisiting brittle fracture as an energy minimization problem. *Journal of the Mechanics and Physics of Solids*, 46(8), 1319–1342.
- [44] Chew, H. B., Hong, S., & Kim, K.-S. (2009). Cohesive zone laws for void growth—II. Numerical field projection of elasto-plastic fracture processes with vapor pressure. *Journal of the Mechanics and Physics of Solids*, 57(8), 1374–1390.
- [45] Hong, S., Chew, H. B., & Kim, K.-S. (2009). Cohesive-zone laws for void growth—I. Experimental field projection of crack-tip crazing in glassy polymers. *Journal of the Mechanics and Physics of Solids*, *57*(8), 1357–1373.

- [46] Kim, H.-G., Chew, H. B., & Kim, K.-S. (2012). Inverse extraction of cohesive zone laws by field projection method using numerical auxiliary fields. *International Journal for Numerical Methods in Engineering*, *91*(5), 516–530.
- [47] Chew, H. B. (2013). Inverse extraction of interfacial tractions from elastic and elastoplastic far-fields by nonlinear field projection. *Journal of the Mechanics and Physics of Solids*, 61(1), 131–144.
- [48] Chew, H. B. (2014). Cohesive zone laws for fatigue crack growth: Numerical field projection of the micromechanical damage process in an elasto-plastic medium. *International Journal of Solids and Structures*, *51*(6), 1410–1420.
- [49] Tran, H., Gao, Y. F., & Chew, H. B. (2022). An inverse method to reconstruct crack-tip cohesive zone laws for fatigue by numerical field projection. *International Journal of Solids and Structures*, 239–240, 111435.
- [50] Negri, M., & Paolini, M. (2001). Numerical minimization of the Mumford-Shah functional. *Calcolo*, 38(2), 67–84.
- [51] Fraternali, F. (2007). Free discontinuity finite element models in two-dimensions for inplane crack problems. *Theoretical and Applied Fracture Mechanics*, 47(3), 274–282.
- [52] Schmidt, B., Fraternali, F., & Ortiz, M. (2009). Eigenfracture: An eigendeformation approach to variational fracture. *Multiscale Modeling and Simulation*, 7(3), 1237–1266.
- [53] Bourdin, B., & Chambolle, A. (2000). Implementation of an adaptive finite-element approximation of the Mumford-Shah functional. *Numerische Mathematik*, 85(4), 609–646.
- [54] Sargado, J. M., Keilegavlen, E., Berre, I., & Nordbotten, J. M. (2018). High-accuracy phase-field models for brittle fracture based on a new family of degradation functions. *Journal of the Mechanics and Physics of Solids*, 111, 458–489.
- [55] Khodadadian, A., Noii, N., Parvizi, M., Abbaszadeh, M., Wick, T., & Heitzinger, C. (2020). A Bayesian estimation method for variational phase-field fracture problems. *Computational Mechanics*, 66(4), 827–849.
- [56] Miehe, C., Teichtmeister, S., & Aldakheel, F. (2016). Phase-field modelling of ductile fracture: A variational gradient-extended plasticity-damage theory and its micromorphic regularization. *Philosophical Transactions of the Royal Society A: Mathematical, Physical and Engineering Sciences*, 374(2066), 20150170.
- [57] Dittmann, M., Aldakheel, F., Schulte, J., Wriggers, P., & Hesch, C. (2018). Variational phase-field formulation of non-linear ductile fracture. *Computer Methods in Applied Mechanics and Engineering*, 342, 71–94.
- [58] Zhuang, X., Zhou, S., Sheng, M., & Li, G. (2020). On the hydraulic fracturing in naturally-layered porous media using the phase field method. *Engineering Geology*, 266, 105306.
- [59] de Borst, R., & Verhoosel, C. V. (2016). Gradient damage vs phase-field approaches for fracture: Similarities and differences. *Computer Methods in Applied Mechanics and Engineering*, 312, 78–94.
- [60] Moës, N., Dolbow, J., & Belytschko, T. (1999). A finite element method for crack growth without remeshing. *International Journal for Numerical Methods in Engineering*, 46(1), 131–150.
- [61] García, I. G., Paggi, M., & Mantič, V. (2014). Fiber-size effects on the onset of fiber—matrix debonding under transverse tension: A comparison between cohesive zone and finite fracture mechanics models. *Engineering Fracture Mechanics*, 115, 96–110.
- [62] Miehe, C., Hofacker, M., Schänzel, L.-M., & Aldakheel, F. (2015). Phase field modeling of fracture in multi-physics problems. Part II. Coupled brittle-to-ductile failure criteria and

- crack propagation in thermo-elastic—plastic solids. *Computer Methods in Applied Mechanics and Engineering*, 294, 486–522.
- [63] Miehe, C., Schänzel, L.-M., & Ulmer, H. (2015). Phase field modeling of fracture in multiphysics problems. Part I. Balance of crack surface and failure criteria for brittle crack propagation in thermo-elastic solids. *Computer Methods in Applied Mechanics and Engineering*, 294, 449–485.
- [64] Chandra, N., Li, H., Shet, C., & Ghonem, H. (2002). Some issues in the application of cohesive zone models for metal–ceramic interfaces. *International Journal of Solids and Structures*, 39(10), 2827–2855.
- [65] Dong, J., Chen, M., Jin, Y., Hong, G., Zaman, M., & Li, Y. (2019). Study on micro-scale properties of cohesive zone in shale. *International Journal of Solids and Structures*, *163*, 178–193.
- [66] Chew, H. B., Guo, T. F., & Cheng, L. (2007). Pressure-sensitive ductile layers I. Modeling the growth of extensive damage. *International Journal of Solids and Structures*, 44(7), 2553–2570.
- [67] Chew, H. B., Guo, T. F., & Cheng, L. (2007). Pressure-sensitive ductile layers II. 3D models of extensive damage. *International Journal of Solids and Structures*, 44(16), 5349–5368.

Figure Captions

- **Figure 1**: (a) Schematic of a sharp crack (left) versus a diffuse crack (right), S, in a deformable body Ω . (b) Schematic of a small-scale yielding, boundary layer model, governed by a phase-field constitutive relation, with a centerline crack (red) introduced through the phase-field damage parameter $\phi = 1$. (c) Finite element mesh of the small-scale yielding model. (d) Close-up view of the highly refined mesh close to the initial crack-tip.
- **Figure 2**: Effects of $G_c/(ED)$ with $I_c/D = 4$ (a) and I_c/D with $G_c/(ED) = 0.015$ (b) on the fracture resistance (R-) curves. Values of $G_c/(ED)$ corresponds to the fracture initiation toughness and are denoted by square symbols.
- **Figure 3:** Contours of the von Mises stress, σ_e , and the phase-field damage variable, ϕ , for three combinations of $G_c/(ED)$ and I_c/D , and at three crack growth instances, $\Delta \alpha/D = 5$, 40, and 80.
- Figure 4: Evolution of the process zone size, as quantified by ϕ , centered on the current cracktip for three combinations of $G_c/(ED)$ and l_c/D , and at three crack growth instances, $\Delta a/D = 5$, 40, and 80.
- Figure 5: Cohesive traction (a), cohesive separation (b), and phase-field damage distributions (c) at $\Delta a/D = 25$ with $l_c/D = 4$ for various $G_c/(ED)$. Schematic of an equivalent zero-thickness cohesive zone law embedded within a linear elastic body in inset in (b).
- **Figure 6**: Cohesive traction (a), cohesive separation (b), and phase-field damage distributions (c) at $\Delta a/D = 25$ with $G_c/(ED) = 0.015$ for various I_c/D .
- Figure 7: Equivalent crack-tip cohesive zone laws in a linear elastic body representing the phase-field damage at $\Delta a/D = 25$ for various $G_c/(ED)$ with $I_c/D = 4$ (a) and various I_c/D with $I_c/D = 0.015$ (b).
- **Figure 8**: Evolution of phase field damage variable (red), ϕ , versus proportion of cohesive energy dissipated (black), Γ_s/Γ , as a function of cohesive separation, δ_2/D , across various l_c/D and $G_c/(ED)$.
- Figure 9: Evolution of the equivalent crack-tip cohesive zone laws with increasing $\Delta a/D$ across various combinations of l_c/D and $G_c/(ED)$.

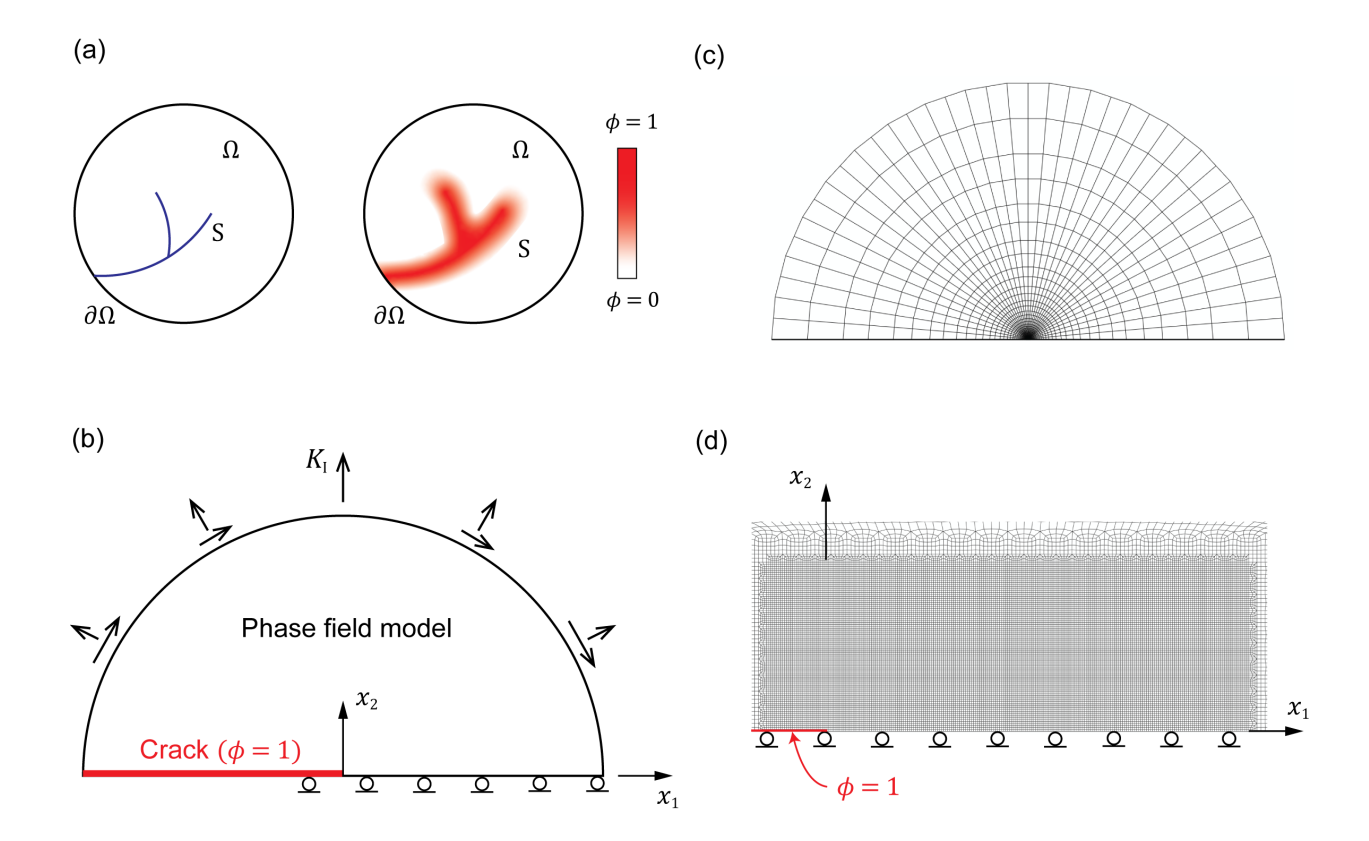


Figure 1: (a) Schematic of a sharp crack (left) versus a diffuse crack (right), S, in a deformable body Ω . (b) Schematic of a small-scale yielding, boundary layer model, governed by a phase-field constitutive relation, with a centerline crack (red) introduced through the phase-field damage parameter $\phi = 1$. (c) Finite element mesh of the small-scale yielding model. (d) Close-up view of the highly refined mesh close to the initial crack-tip.

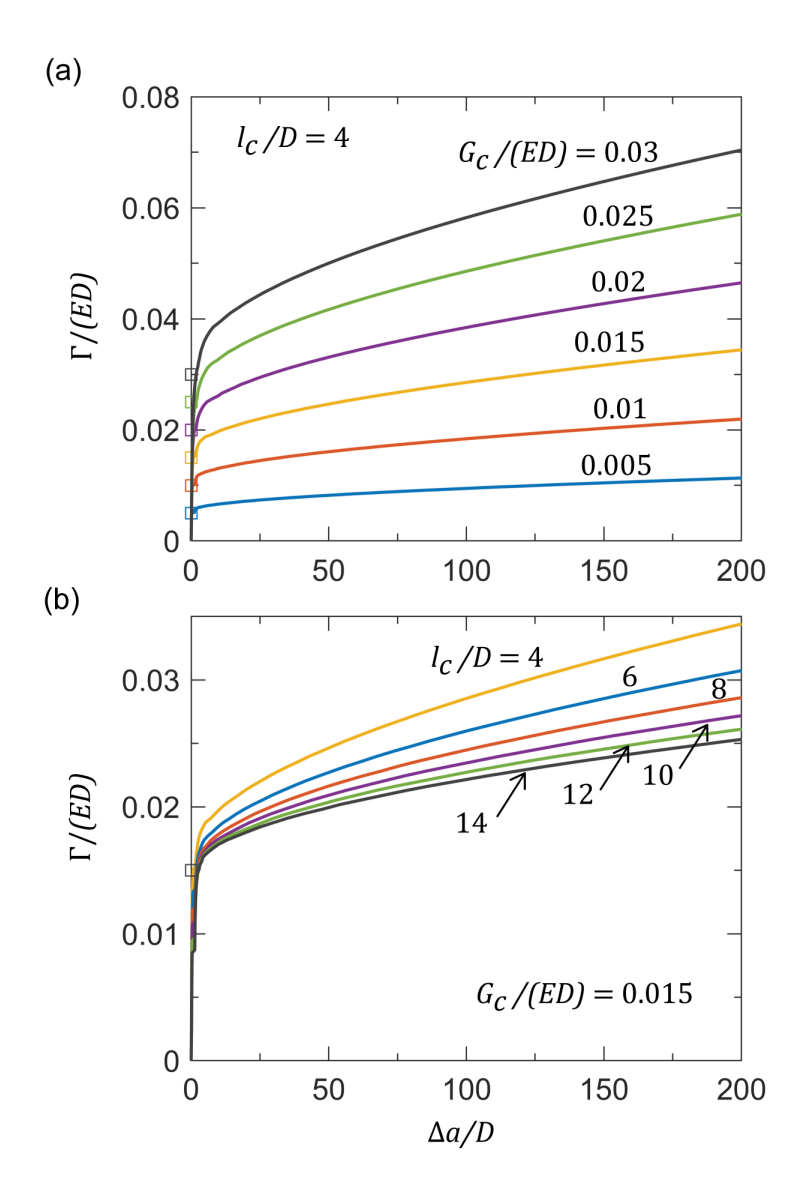


Figure 2: Effects of $G_c/(ED)$ with $I_c/D = 4$ (a) and I_c/D with $G_c/(ED) = 0.015$ (b) on the fracture resistance (R-) curves. Values of $G_c/(ED)$ corresponds to the fracture initiation toughness and are denoted by square symbols.

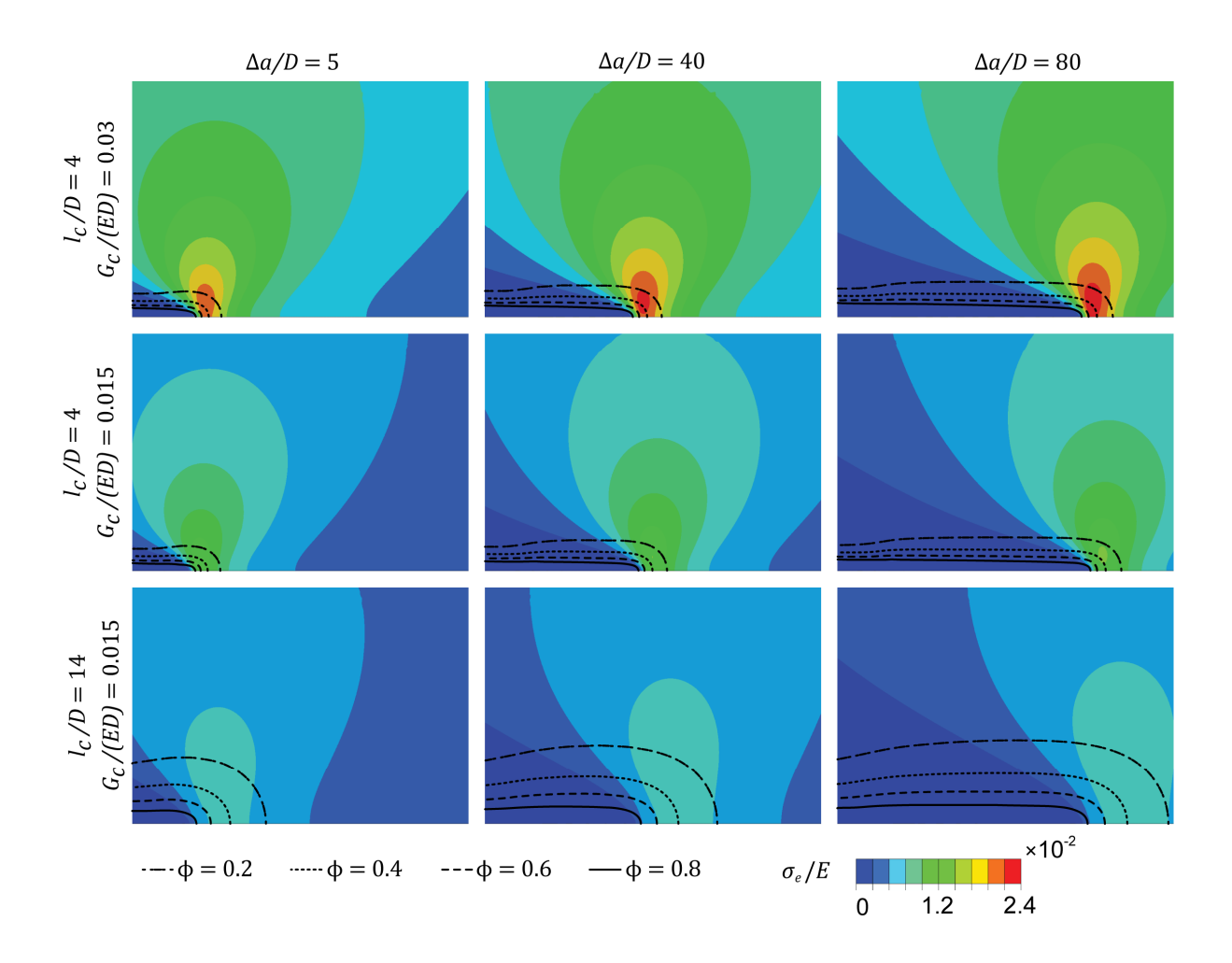


Figure 3: Contours of the von Mises stress, σ_e , and the phase-field damage variable, ϕ , for three combinations of $G_c/(ED)$ and I_c/D , and at three crack growth instances, $\Delta a/D = 5$, 40, and 80.

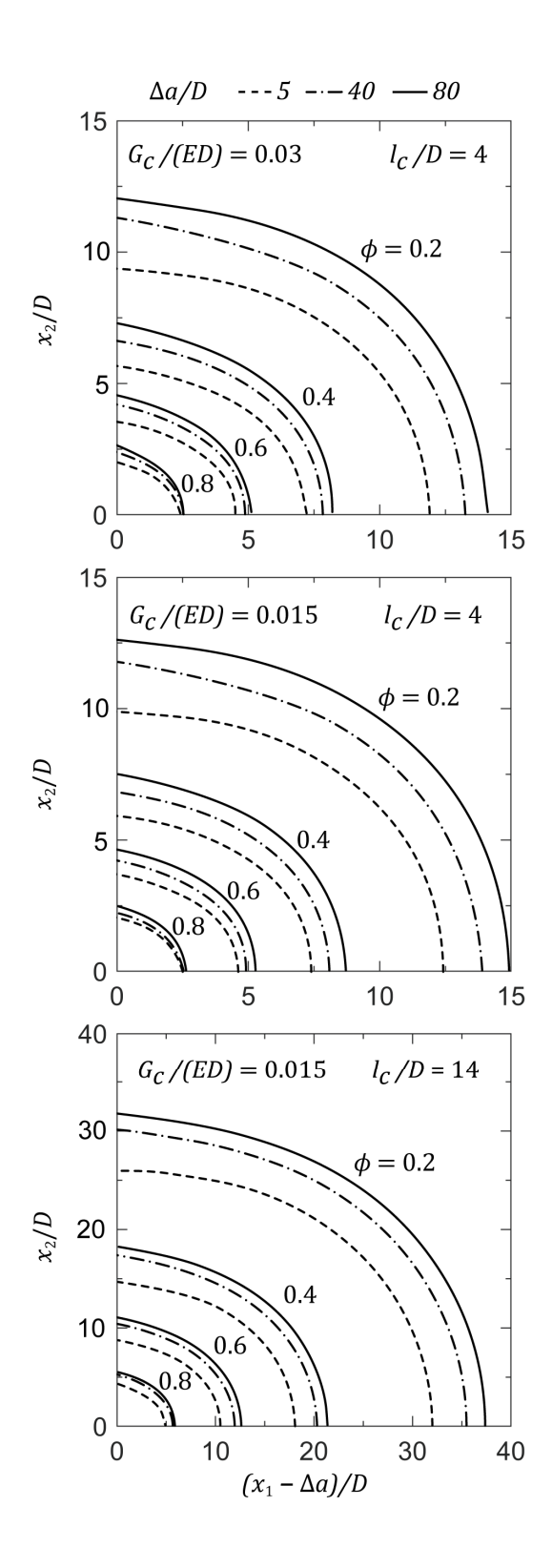


Figure 4: Evolution of the process zone size, as quantified by ϕ , centered on the current crack-tip for three combinations of $G_c/(ED)$ and I_c/D , and at three crack growth instances, $\Delta a/D = 5$, 40, and 80.

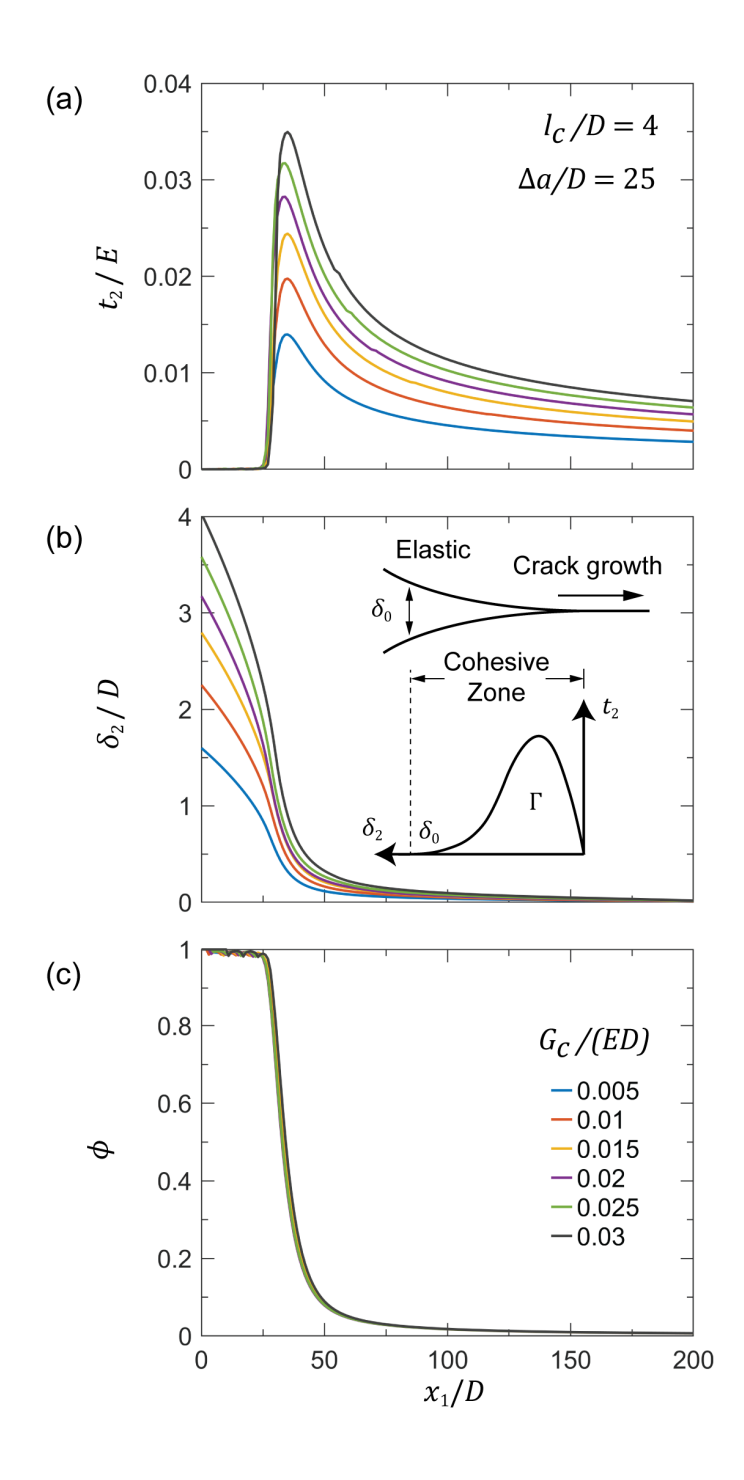


Figure 5: Cohesive traction (a), cohesive separation (b), and phase-field damage distributions (c) at $\Delta a/D = 25$ with $l_c/D = 4$ for various $G_c/(ED)$. Schematic of an equivalent zero-thickness cohesive zone law embedded within a linear elastic body in inset in (b).

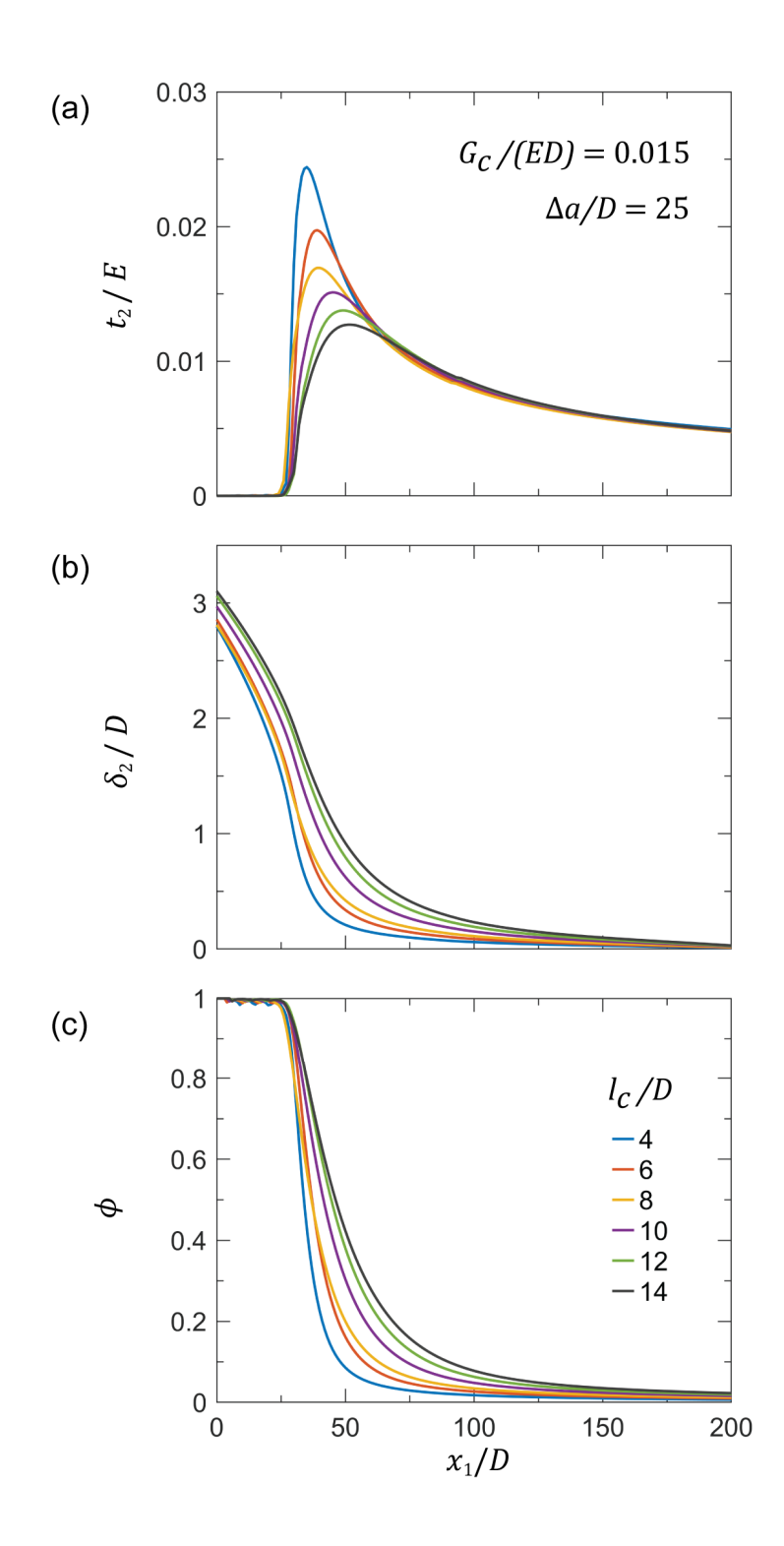


Figure 6: Cohesive traction (a), cohesive separation (b), and phase-field damage distributions (c) at $\Delta a/D = 25$ with $G_c/(ED) = 0.015$ for various I_c/D .

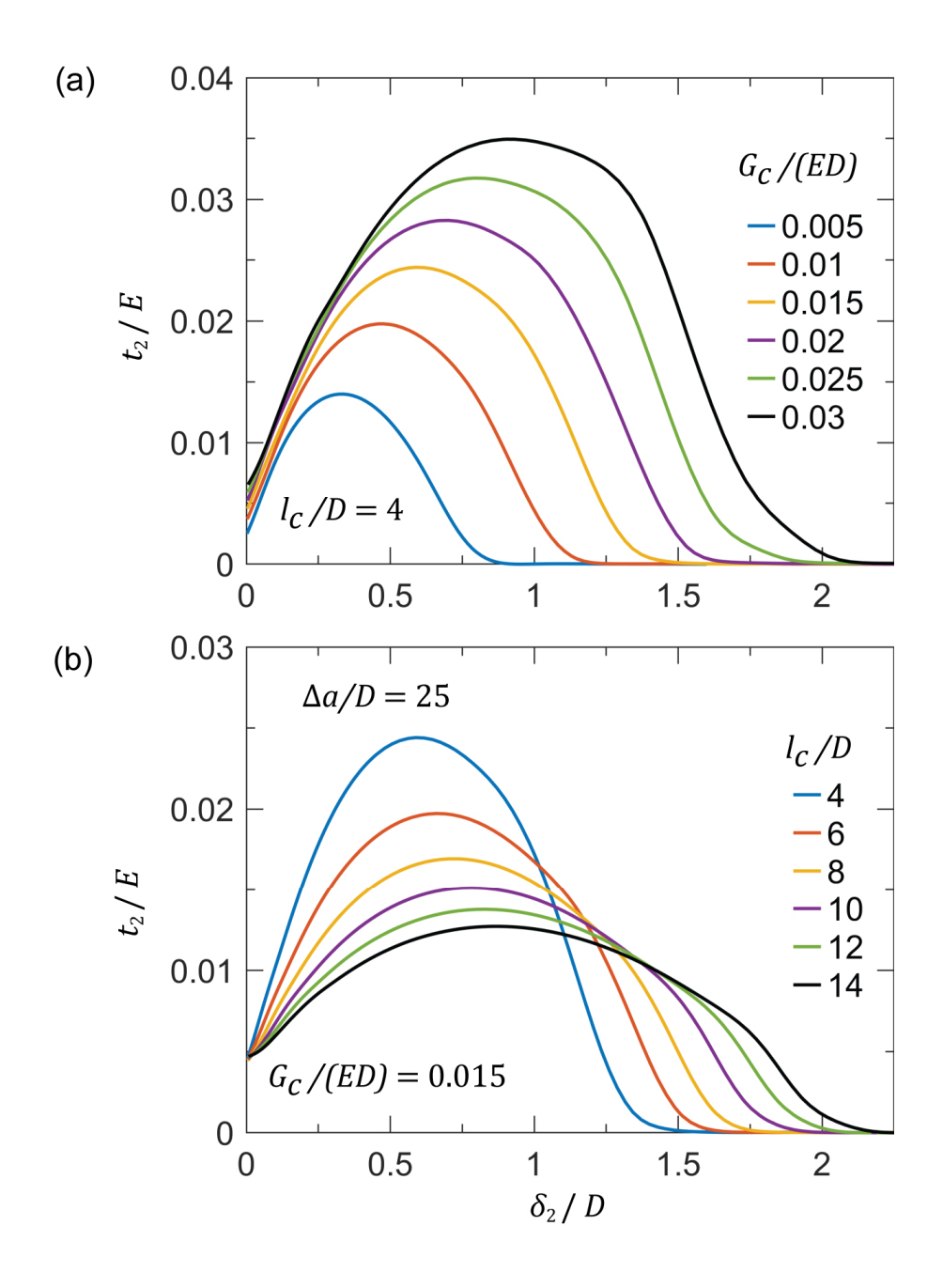


Figure 7: Equivalent crack-tip cohesive zone laws in a linear elastic body representing the phase-field damage at $\Delta a/D = 25$ for various $G_c/(ED)$ with $I_c/D = 4$ (a) and various I_c/D with $I_c/D = 0.015$ (b).

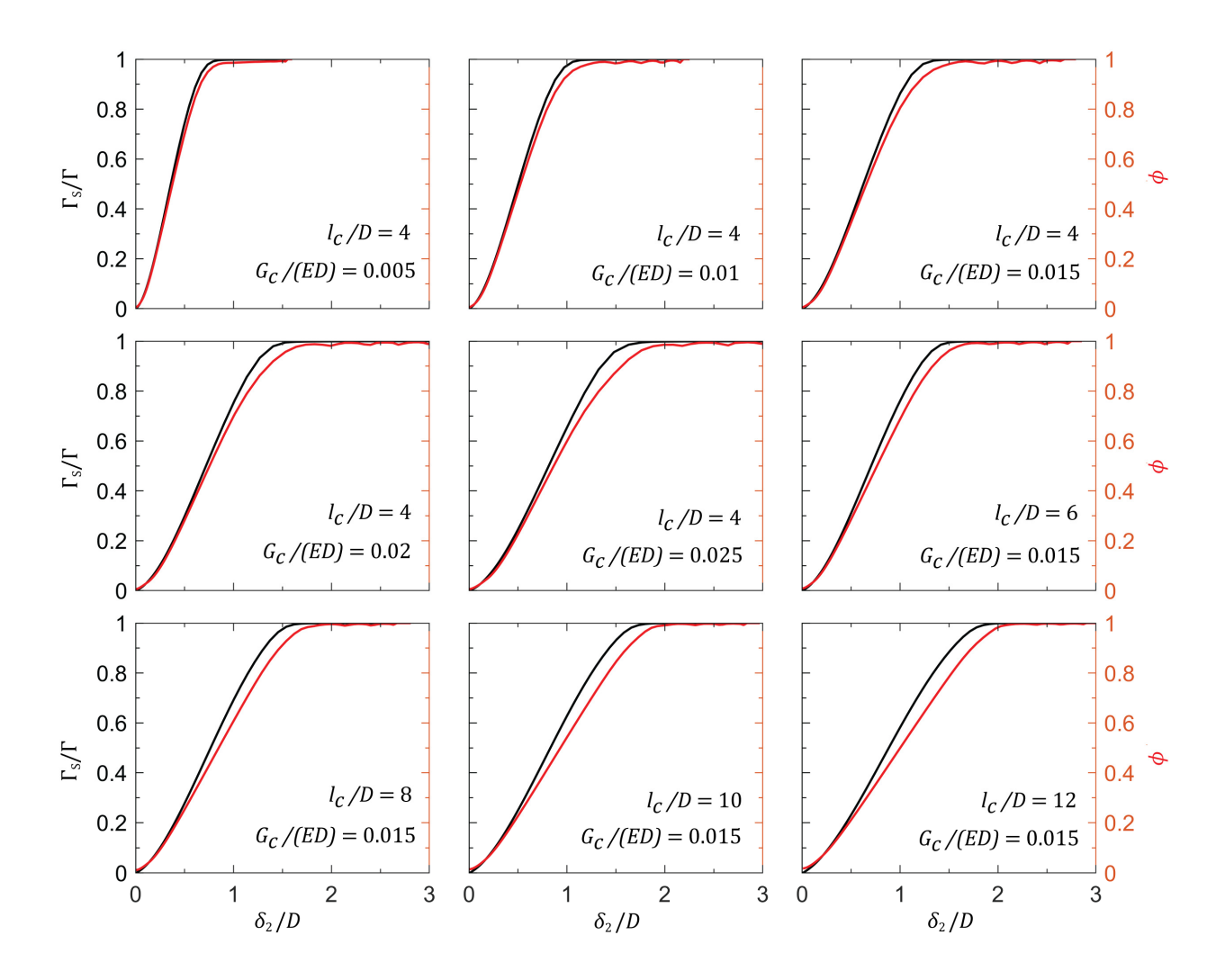


Figure 8: Evolution of phase field damage variable (red), ϕ , versus proportion of cohesive energy dissipated (black), Γ_s/Γ , as a function of cohesive separation, δ_2/D , across various l_c/D and $G_c/(ED)$.

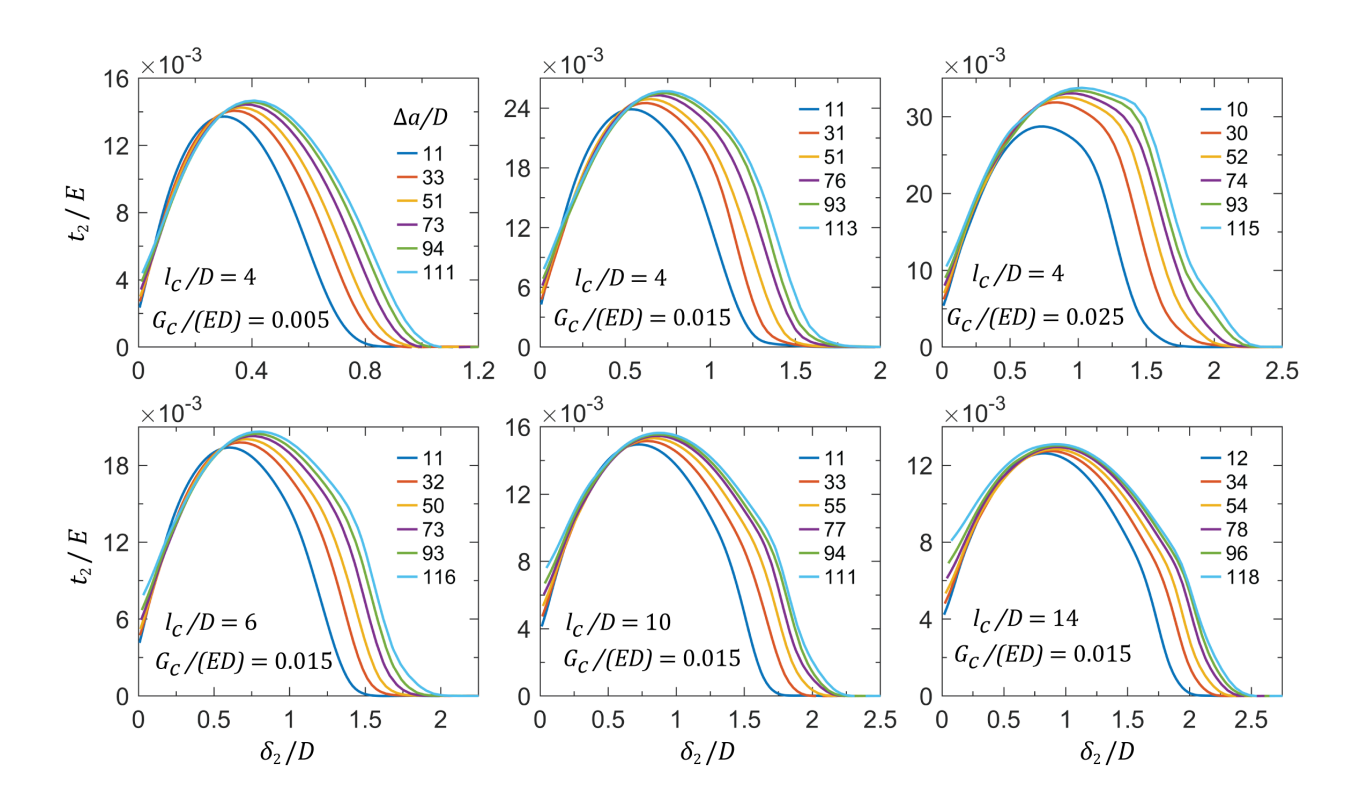


Figure 9: Evolution of the equivalent crack-tip cohesive zone laws with increasing $\Delta a/D$ across various combinations of l_c/D and $G_c/(ED)$.